Polarization control of the property of dopants in semiconductors

Hang Zang,[1] Zhiming Shi,[1] Mingrui Liu,[1] Yuping Jia,[1] Ke Jiang,[1] Xiaojuan Sun,[1,*] and Dabing Li[1,2,†]

[1]*Key Laboratory of Luminescence Science and Technology, Chinese Academy of Sciences & State Key Laboratory of Luminescence and Applications, Changchun Institute of Optics, Fine Mechanics and Physics, Chinese Academy of Sciences, Changchun 130033, China*

[2]*Center of Materials Science and Optoelectronics Engineering, University of Chinese Academy of Sciences, Beijing 100049, China*

(Received 13 January 2024; revised 22 April 2024; accepted 9 July 2024; published 24 July 2024)

Dopants can bring new functionalities to semiconductor materials; therefore, it is desirable to optimize the properties of dopants to achieve better performance. In this work, we demonstrate that the property of a dopant can be tuned to various extents by the polarization effect. We have proposed a mix-phase AlN/ScN superlattice system as substrate, whose built-in polarization is an order of magnitude larger than that in a AlN/GaN superlattice. Taking the 3*d* transition metal as a dopant, we show by first-principles calculations that the stable electronic configuration of individual dopants and the spin-exchange interaction between different dopants can be effectively controlled by the polarization effect. Specifically, for the case of Co_{Sc}, the relative stability between the 0 μ_B ($t_{2g}^6 e_g^0$) and the 4 μ_B ($t_{2g}^4 e_g^2$) magnetic states can be tuned by varying the doping positions along the polarization direction. For the case of V_{Al} with $e^2 t_2^0$ electronic configuration, the ferromagnetic interaction between half-filled e states and empty t_2 states can be enhanced when the adjacent V_{Al} dopants are at inequivalent doping positions along the polarization direction. These results show that the polarization effect has a significant impact on dopant properties in semiconductors. Further, as the AlN/ScN material system is compatible with existing complementary metal-oxide-semiconductor (CMOS) back-end processes, it can serve as a versatile platform to obtain large polarization fields and thus can achieve effective polarization control of dopant properties experimentally.

DOI: 10.1103/PhysRevB.110.035206

I. INTRODUCTION

Incorporating intentional impurities into a material is an effective method for tuning its physical properties [1]. For traditional semiconductors, doping donors or acceptors into these materials can shift the Fermi level and lead to the presence of mobile free carriers for electronic conductance [2], which is crucial for achieving electron-pumped nanodevices. With the development of experimental methods such as single-ion implantation techniques [3], it has become possible to incorporate various elements into a material, thereby introducing new functionalities. For example, dilute magnetism [4–6] can be achieved by doping magnetic ions into semiconductors such as GaAs [7], ZnO [8], and GaN [9], where one of the spin-polarized states dominates at the Fermi level, allowing for the production of spin-polarized currents suitable for spintronic devices [10,11]. Rare-earth elements cover a broad optical spectral range, and they can be doped into host materials for photoluminescence and related applications, including lighting, electronic displays, lasers, and biological labeling [12]. Defects with isolated energy levels insulated from the band edges of wide-band-gap semiconductors can serve as single-photon emitters for qubits [13,14]. In these applications, the relative position between the energy levels induced by dopants or defects and the host bands plays a crucial role.

In bulk semiconductor materials, a polarization effect occurs when the positive and negative charge centers do not coincide, which can induce a difference in electrostatic potential along the polarization direction. At the surface and interfaces of semiconductors, this polarization effect exhibits discontinuous characteristics, exerting pronounced influences on electronic structures and charge distributions, and leading to band bending [15]. The polarization discontinuity effect, when coupled with dopants, offers a different avenue for tuning dopant properties.

The influence of polarization discontinuity near the surface on dopants is particularly evident in the case of nitrogen-vacancy (NV) centers in diamond, which have garnered considerable attention due to their unique magnetic and optical properties [13]. Experimental investigations have revealed that surface dipoles play a crucial role in determining the relative stabilities of neutral NV^0 and negative NV^- states near the diamond surface. Specifically, NV^- tends to be stable near oxygen-saturated surfaces, whereas NV^0 is favored near hydrogen-saturated surfaces [16–18]. This development marks a significant stride towards engineering NV centers near the diamond surface. For wide-band-gap nitride semiconductors, the polarization discontinuity effect has been used as a tool to enhance *p*-doping efficiency. Specifically, the polarization effect induced by the $Al_xGa_{1-x}N/Al_yGa_{1-y}N$ superlattice structure induces the bending of valence bands around the interface, resulting in a reduction of the acceptor activation energy [19–22]. Additionally, Simon *et al.* [23] developed a technology for growing AlGaN material with a reduced Al component along the [0001] direction of AlGaN. Instead of sharp superlattice heterojunctions, they achieved an Al component gradient and thereby a polarization gradient, which can benefit the activation of

*Contact author: sunxj@ciomp.ac.cn
†Contact author: lidb@ciomp.ac.cn

acceptors, and further achieved a high hole concentration of 2×10^{18} cm^{-3}.

Understanding the interdependence between polarization and dopants holds great promise for enabling precise control over material functionalities for diverse applications. So far, the polarization effect has primarily been utilized to adjust the properties of dopants whose energy levels are close to the host band edge. However, its regulatory impact on dopants with deep energy levels remains relatively unexplored. In this work, we demonstrate the higher feasibility of the polarization effect for tuning the dopant property in semiconductors. We have systematically studied the effect of polarization on the stable electronic configurations of a dopant, which are directly related to the relative position between the dopant energy level and host band edges. We use a mix-phase AlN/ScN superlattice as the host material, as we show later that it possesses a sufficiently large built-in electric polarization field. The 3*d* transition-metal (TM) series from Ti to Zn is chosen as the dopants. The effect of polarization on the electronic structure of individual dopants and the interaction between dopant pairs are discussed in detail. Through systematic analysis, we elucidate the impact of polarization on individual dopants and the interactions between dopant pairs, shedding light on the potential of polarization engineering for tailored semiconductor materials.

II. COMPUTATION DETAILS

The calculations are performed based on density functional theory using the VASP package [24,25]. We employ the projector-augmented wave (PAW) pseudopotential [26,27] with an energy cutoff of 500 eV. We have investigated the effect of exchange-correlation functionals on the polarization property and the energy of different transition metals. The functionals used include the local density approximation (LDA), the generalized gradient approximation (GGA), and the meta-GGA functionals. For LDA, we use the Ceperley-Alder (CA) [28] functional. For GGA, we use the Perdew-Burke-Ernzerhof (PBE) functional [29]. For meta-GGA, we use the strongly constrained and appropriately normed (SCAN) functional [30]. Previous theoretical investigations [31] have shown that the LDA and GGA functionals tend to induce delocalized behavior in transition metals, whereas the meta-GGA functional tends to produce localized behavior. In the main text, we present results based on the PBE functional, while results based on other exchange-correlation functionals are presented in the Supplemental Material [32]. Fixed-spin self-consistent calculations are performed, and the constrained total magnetic moment state is achieved by separately varying the Fermi levels of the spin-up and spin-down electrons. For all the calculations, the *K*-mesh value is set to be $0.05 \times 2\pi/$Å, and the atomic positions are relaxed until the forces are less than 0.01 eV/Å.

The formation energy of a transition-metal dopant is defined as [33]

$$E_f(X^q) = E_{\text{tot}}(X^q) - E_{\text{tot}}(\text{host}) - \sum_i n_i \mu_i + qE_F + \Delta^q. \tag{1}$$

Here, $E_{\text{tot}}(X^q)$ represents the total energy of the supercell containing a dopant X at the charge state of q, $E_{\text{tot}}(\text{host})$ is the total energy of the host semiconductor without dopants, n_i is the number of atoms of type i that have been added to ($n_i > 0$) or removed from ($n_i < 0$) the host, μ_i is the corresponding chemical potential for atom i, E_F is the Fermi level referenced to the valence band maximum (VBM), and Δ^q is the correction term for the finite-cell size effect on the total energies of the charged defects [34,35].

III. RESULTS AND DISCUSSION

A. Polarization effect in the AlN/ScN superlattice

We begin by examining the polarization property of the AlN/ScN superlattice. The freestanding superlattice structure is considered, with both the lattice constant and internal coordinates relaxed. Different phases of the AlN/ScN superlattice are investigated, as previous studies have indicated that it can exist in either a wurtzite or a wurtzite/rock-salt mix-phase structure [36–38]. Notably, such mix-phase structures have also been observed in space-confined nitride materials [39,40] and heteroepitaxial nitride material systems [41].

As a superlattice structure, interfaces between different regions create a dipole discontinuity [42,43]. In this study, we demonstrate the corresponding built-in electric field polarization by calculating the atomic core levels (E^{CL}) [44,45]. Utilizing the core level of N_{1s} as the reference, the electric field is determined by fitting the slope of the core level difference (ΔE^{CL}) of N atoms from different layers with respect to their distance (Δz) along the polarization direction (which is perpendicular to the interface). The results for the wurtzite AlN/GaN and mix-phase AlN/ScN superlattices are shown in Figs. 1(a) and 1(b), and the results for wurtzite AlN/ScN superlattice are shown in Fig. S1(a) in the Supplemental Material [32]. Remarkably, the calculated polarization field in the mix-phase AlN/ScN is an order of magnitude larger than that of both the wurtzite AlN/GaN and wurtzite AlN/ScN superlattices.

To gain insight into the significant polarization field observed in the mix-phase AlN/ScN superlattice, we employed a slab model to investigate the charge transfer between different regions. The results are presented in Fig. S2 in the Supplemental Material [32]. Our findings reveal a larger planar and macroscopic-averaged charge density difference at the interfaces in the mix-phase AlN/ScN superlattice compared to the wurtzite AlN/GaN and wurtzite AlN/ScN superlattices. This pronounced difference contributes to the relatively large polarization field observed in the mix-phase structure. Another noteworthy distinction in the polarization field between the AlN/GaN and AlN/ScN superlattices is the position of the maximum N_{1s} core level. In the wurtzite AlN/GaN superlattice, this position is situated in the AlN region, whereas in both the wurtzite and mix-phase AlN/ScN superlattices, it resides in the ScN region. This should arise from the distinct nature of the valence orbitals of Sc (*d* orbital) and Ga (*p* orbital), as the maximum position of the N_{1s} core level remains consistent for AlN/ScN superlattices with different (wurtzite or mix-phase) crystal structures. Additionally, Fig. S3 in the Supplemental Material [32] demonstrates that a large polarization field

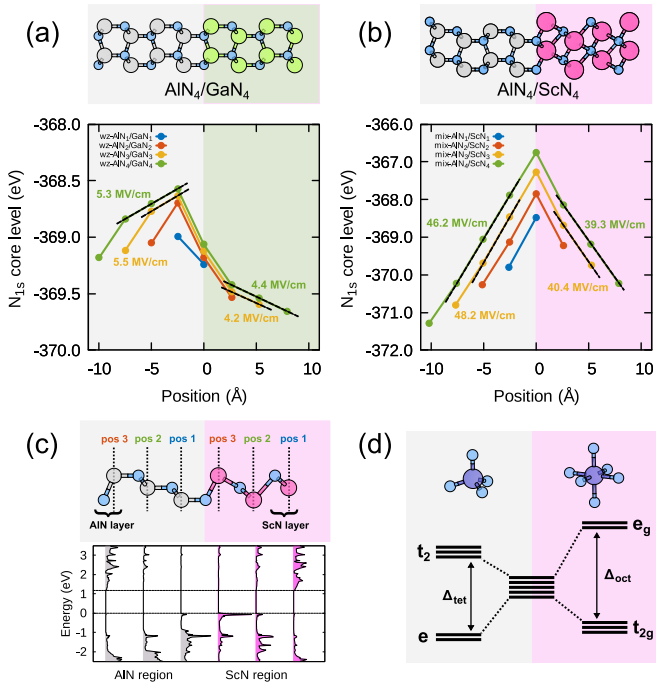

FIG. 1. Atomic structure and N_{1s} binding energies for (a) wurtzite AlN_n/GaN_n and (b) mix-phase AlN_n/ScN_n superlattices. (c) Unit-cell structure of a mix-phase AlN_3/ScN_3 superlattice and layer-resolved density of states. The valence band maximum is set to 0. (d) Schematic representation of TM d-orbital splittings under ideal tetrahedral and octahedral coordination. Al, Ga, Sc, N, and TM atoms are depicted by gray, green, pink, blue, and purple balls, respectively.

exists in the mix-phase AlN/ScN superlattice regardless of the stacking sequence in the AlN region.

The large polarization field in the mix-phase AlN/ScN superlattice strongly influences its electronic structure. Figure 1(c) illustrates the layer-projected density of states (DOS) for the mix-phase AlN_3/ScN_3. Notably, the DOS exhibits a distinct bending for different layers. The band gap of the mix-phase AlN_n/ScN_n is also strongly influenced by the polarization field, as shown in Table S1 in the Supplemental Material [32], and the band gap dramatically reduces as the layer number n of the mix-phase AlN_n/ScN_n increases. For comparison, Fig. S1(b) presents the layer-projected DOS results for wurtzite AlN_3/ScN_3. In contrast to the mix-phase structure, the relatively weak polarization field in the wurtzite AlN_3/ScN_3 superlattice results in minimal variation in the layer-projected DOS, regardless of the layer's position.

To assess the influence of exchange-correlation functionals on the electronic structure, we performed core level and band-gap calculations for mix-phase AlN_n/ScN_n using both LDA and SCAN functionals. The results are summarized in Fig. S9 and Table S1 in the Supplemental Material [32]. Remarkably, we observe that the polarization field strength as well as the band-gap reduction feature with the increase of n remain consistent with the results obtained using the PBE functional. This consistency indicates that the inherent built-in field property can be reliably reproduced by the PBE functional.

To demonstrate that polarization in semiconductors can effectively tune the property of a dopant, we have studied the dependence of the total energy as a function of the total magnetic moment of a host material with a dopant incorporated; as the stable magnetic property for a material with a dopant is directly related to the dopant electronic configuration [46,47], which is determined by the relative position between the dopant energy level and the host band edges [48]. We choose the mix-phase AlN_3/ScN_3 superlattice as the host material as it exhibits a large polarization field; the dopants are chosen as the 3d TM series from Ti to Zn.

The TM dopants were modeled by replacing one of the cation atoms in the $3 \times 3 \times 1$ mix-phase AlN_3/ScN_3 supercell with one TM atom, as illustrated in Fig. 1(c), where the labels denote different doping positions of the substitutional TM atom. Due to the polarization field along the direction perpendicular to the superlattice interface, the TM dopants experience unequal doping positions. Doping in the AlN region, denoted by the change from pos1 to pos2 and then to pos3, results in the TM ion sensing a potential that moves toward lower energy levels. Conversely, doping in the ScN region, characterized by the transition from pos1 to pos2 and then to pos3, results in the TM ion sensing a potential that moves toward higher-energy levels.

In the mix-phase AlN_3/ScN_3, the splitting of the TM d states is influenced by the coordination [49,50]. As depicted in Fig. 1(d), in an ideal tetrahedral crystal field, the d states split into a low-energy double degenerate e set and a high-energy triple degenerate t_2 set, with a crystal field splitting energy Δ_{tet}; whereas in an ideal octahedral crystal field, they split into a low-energy triple degenerate t_{2g} set and a high-energy double degenerate e_g set, with a crystal field splitting energy Δ_{oct}. The final electronic configuration of the d states is determined by the relative magnitude between Δ_{tet} (Δ_{oct}) and the positive pairing energy P for a pair of spin-antiparallelized electrons on the same orbital.

B. Property of transition-metal dopant in the AlN region of AlN/ScN superlattice

For TM dopants in the AlN region of the mix-phase AlN_3/ScN_3, the electronic configurations under ideal tetrahedral coordination are depicted in Fig. 2(a). For Ti_{Al}, V_{Al}, Ni_{Al}, Cu_{Al}, and Zn_{Al}, there is one possible stable magnetic configuration, while for Cr_{Al}, Mn_{Al}, Fe_{Al}, and Co_{Al}, there are two possible stable magnetic configurations. To numerically study the electronic structure of TM dopants at different doping positions in the AlN region of mix-phase AlN_3/ScN_3 and the effect of polarization on it, we performed fixed-spin multiplet calculations for the supercell to obtain the total energy curve of the system as a function of its total magnetic moment. Full atomic relaxations were included for all calculations, and the results are shown in Fig. 2(b). It is evident that the energy curves for the same dopant at different doping positions exhibit significant differences.

For Ti_{Al}, V_{Al}, Ni_{Al}, Cu_{Al}, and Zn_{Al}, there exist metastable magnetic moment of 0 μ_B or flat total energy curves between 0 μ_B and the corresponding ideal magnetic states shown in Fig. 2(a). For Cr_{Al}, Mn_{Al}, Fe_{Al}, and Co_{Al}, though multiple stable magnetic moments exist for the ideal case, the numerical

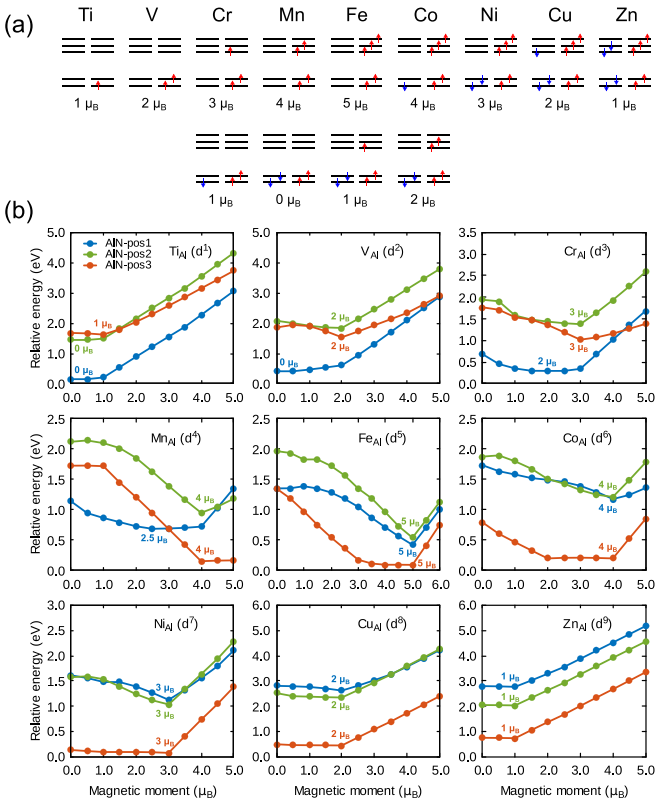

FIG. 2. (a) Electronic configurations for TM dopants under ideal tetrahedral coordination. (b) Relative energy as a function of the total magnetic moment for TM in different doping positions in the AlN region of mix-phase AlN_3/ScN_3. The stable magnetic moment for each case is labeled.

results do not show that the energy curve has multiple stable magnetic moment states; instead, some new stable magnetic moment configuration exists. For Cr_{Al}, it is stable at 2 μ_B at pos1; for Mn_{Al}, it is stable at 2.5 μ_B at pos1 and there exists a flat total curve between 4 and 5 μ_B at pos3; and for Co_{Al}, there exists a flat total energy curve between 2 and 4 μ_B at pos3.

To understand the origin of the different stable magnetic configuration properties of TM dopants, we calculated the corresponding projected density of states (DOS), as depicted in Fig. 3. Observations reveal that for TM dopants from Ti to Zn at the same doping site, the TM d state shifts towards lower-energy levels with increasing atomic number. Furthermore, for the same TM dopant, the relative position between the d state and the valence band maximum (VBM) and conduction band minimum (CBM) band edges of the host material at different doping positions varies, leading to different energy curves at different doping positions, as shown in Fig. 2. Next, we discuss in detail the features of the density of states for TM_{Al} in mix-phase AlN_3/ScN_3.

For Ti_{Al}, the d states of Ti_{Al}-pos1 and Ti_{Al}-pos2 lie above the CBM of the host material, and part of the conduction band state of the host material lies below the Fermi level; the excess electron induced by Ti_{Al}-pos1 is distributed on the host conduction band states, which results in a nonmagnetic configuration; while the e set of d states of Ti_{Al}-pos3 lies around the host CBM in the spin-up channel and below the Fermi level, the excess electron induced by Ti_{Al} is distributed on the spin-up channel of the e state, which results in a 1 μ_B magnetic moment.

For V_{Al}, additionally, we show the density of states for both the 0 and 2 μ_B conditions as depicted in Fig. S4 in the Supplemental Material [32]. It is seen that the d states lie in a relatively lower-energy region in comparison to the case of Ti_{Al}; the whole d states of V_{Al}-pos1 lie above the CBM of the host material and above the Fermi level, which results in a nonmagnetic configuration; while the e set of d states of V_{Al}-pos2 and V_{Al}-pos3 lies around the host CBM and VBM, respectively, and are both below the Fermi level, which results in a 2 μ_B magnetic moment.

For Cr_{Al}, the low-energy e set of d states of Cr_{Al}-pos1 overlaps with the conduction band of the host material; the excess electron induced by Cr_{Al}-pos1 partly distributes on the e set of d states of Cr_{Al}-pos1 and partly on the conduction band states of the host material, in which the latter tends to form a nonmagnetic configuration, which results in a reduced magnetic moment of 2 μ_B; while the high-energy t_2 set of d states of Cr_{Al}-pos2 and Cr_{Al}-pos3 are mixed with the host CBM and VBM states, respectively, the excess electrons induced by Cr_{Al} are distributed on the spin-up channel of the e and t_2 set of d states, which results in a 3 μ_B magnetic moment.

For Mn_{Al}, the high-energy t_2 set of d states of Mn_{Al}-pos1 overlaps with the conduction band of the host material; the excess electron induced by Mn_{Al} distributes around CBM, which results in a reduced magnetic moment of 2.5 μ_B; the t_2 set of d states of Mn_{Al}-pos2 overlaps with the valence band of the host material; the d states in the spin-up channel are occupied by the excess electron induced by Mn_{Al}, which results in a magnetic moment of 4 μ_B; the spin-up channel of the d state is fully occupied for Mn_{Al}-pos3 and part of the VBM electronic state of the host material is unoccupied, resulting in a flat energy curve around 4–5 μ_B.

For Fe_{Al}, the d states of Fe_{Al}-pos1 and Fe_{Al}-pos2 are fully occupied in the spin-up channel and fully unoccupied in the spin-down channel, which results in a stable magnetic moment of 5 μ_B; while the d states of Fe_{Al}-pos3 are fully occupied in the spin-up channel but also partially occupied in the spin-down channel, as compensation the band edges of the host materials are partially unoccupied in the spin-down channel, which again results in a stable magnetic moment of 5 μ_B.

For Co_{Al}, the d states of Co_{Al}-pos1 and Co_{Al}-pos2 are fully occupied in the spin-up channel and partially occupied in the spin-down channel, which results in a stable magnetic moment of 4 μ_B; while for the case of Co_{Al}-pos3, the occupation of d states in the spin-up channel is similar to that of Co_{Al}-pos1 and Co_{Al}-pos2, but it has more electron occupation in the spin-down channel since the valence band states of the host material exhibit a partial nonoccupation feature, where the 4 μ_B magnetic moment is still stable.

For the cases of Ni_{Al}, Cu_{Al}, and Zn_{Al}, they have the stable magnetic moment that is consistent with the ideal case, and the low-energy metastable configurations of 0 μ_B, which can be accounted for by the coupling between the TM d state and the host material band edge for the previous cases of TM_{Al}.

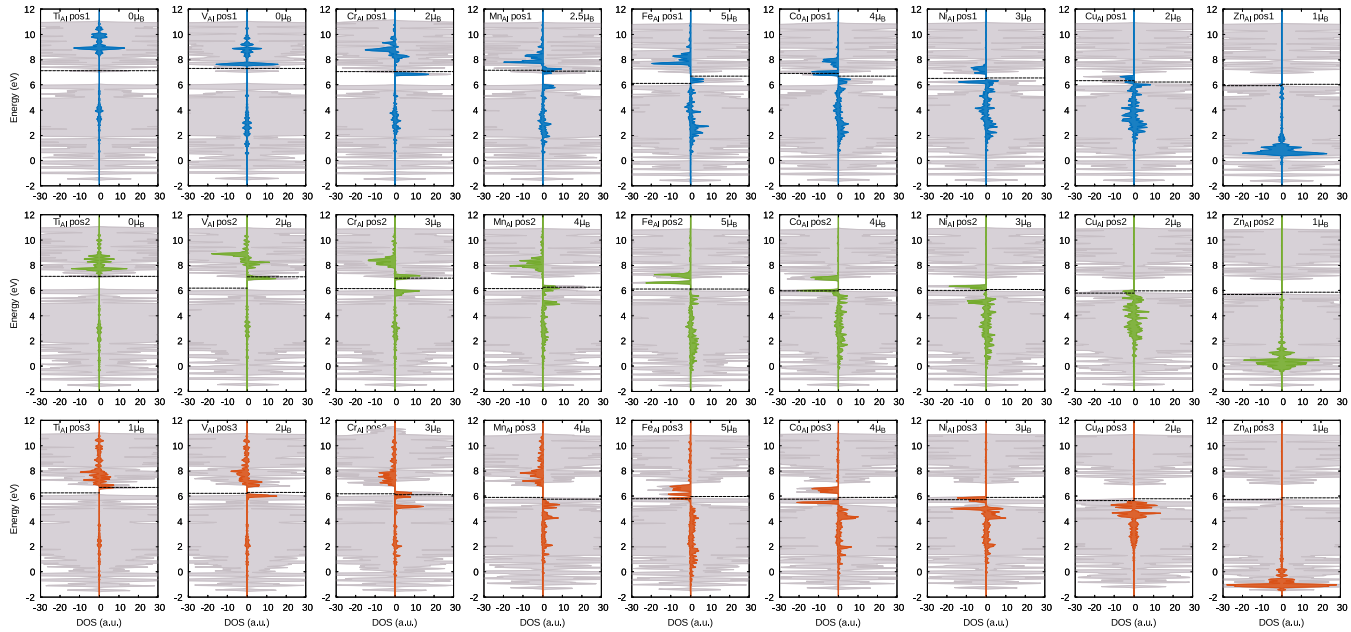

FIG. 3. The total density of states (gray line) and projected density of states of the d orbitals of TM doping in the AlN region of mix-phase AlN_3/ScN_3 at pos1 (blue line), pos2 (green line), and pos3 (red line). The negative and positive values correspond to spin-down and spin-up channels, respectively. The dashed line indicates the Fermi level.

C. Property of transition-metal dopant in the ScN region of AlN/ScN superlattice

For the case of the TM dopant in the ScN region of the mix-phase AlN_3/ScN_3, the results are depicted in Fig. 4. As illustrated in Fig. 4(a), Ti_{Sc}, V_{Sc}, Cr_{Sc}, Cu_{Sc}, and Zn_{Sc} exhibit a single stable magnetic configuration, whereas Mn_{Sc}, Fe_{Sc}, Co_{Sc}, and Ni_{Sc} exhibit two stable magnetic configurations. Notably, these results may differ from those obtained under tetrahedral coordination. Similar to the situation when the TM is doped into the AlN region, the potential energy curve of the energy versus magnetic moment shows obvious differences at different doping sites. This is obvious for the case of Co_{Sc}: for Co_{Sc}-pos1, its most stable magnetic moment is 4 μ_B; for Co_{Sc}-pos3, its most stable magnetic moment is 0 μ_B; while for Co_{Sc}-pos2, the 0 and 4 μ_B magnetic moments are two stable magnetic configurations with close energy.

To understand the mechanism of different stable magnetic moments for TM at different doping sites in the ScN region, we have calculated the corresponding projected density of states; the results for all the dopants are shown in Fig. S5 in the Supplemental Material [32]. Focusing on the case of Co_{Sc}, the density of states results at 0 and 4 μ_B magnetic moments are shown in Fig. 5. The relative position of the Co_{Sc} d states at different positions aligns with the polarization direction in the ScN region of mix-phase AlN_3/ScN_3. It is seen that for the 0 μ_B magnetic configuration of Co_{Sc}-pos1, Co_{Sc}-pos2, and Co_{Sc}-pos3, the d states of Co_{Sc} also exhibit a nonmagnetic feature, where the spin-up and spin-down channels exhibit the same profile and occupancy. For the 4 μ_B magnetic configuration of Co_{Sc}-pos1, Co_{Sc}-pos2, and Co_{Sc}-pos3, the d states in the spin-up channel are fully occupied, while the low-energy d states in the spin-down channel are partially occupied.

For TM dopants in octahedral coordination with an electron number larger than 3, the crystal field splitting energy Δ_{oct} tends to hinder the electron from forming a high magnetic moment configuration, while the pairing energy P tends to hinder the electron from forming a low magnetic moment configuration. For Co_{Sc}-pos1, the high-energy e_g set of d states of Co are mixed with the valence band of the host material and is possibly occupied; then the hindrance of Δ_{oct} is surmounted and the pairing energy P determines the magnetic configuration, thereby resulting in a high-spin $t^3_{2g\uparrow}e^2_{g\uparrow}t^1_{2g\downarrow}e^0_{g\downarrow}$ configuration. For Co_{Sc}-pos2, the low-energy t_{2g} set of d states of Co is mixed with the valence band of the host material and the high-energy e_g set of d states of Co is mixed with the conduction bands of the host material; the crystal field splitting energy Δ_{oct} and pairing energy P play a similar role, which results in the low-spin $t^3_{2g\uparrow}e^0_{g\uparrow}t^3_{2g\downarrow}e^0_{g\downarrow}$ and high-spin $t^3_{2g\uparrow}e^2_{g\uparrow}t^1_{2g\downarrow}e^0_{g\downarrow}$ configurations having comparable energies. For Co_{Sc}-pos3, the low-energy t_{2g} set of d states is mainly mixed with the conduction bands of the host material, and the occupancy of the high-energy e_g requires excess energy, which results in the low magnetic configuration of $t^3_{2g\uparrow}e^0_{g\uparrow}t^3_{2g\downarrow}e^0_{g\downarrow}$ being stable.

To verify the obtained results in this section and the previous section, the LDA and SCAN functionals are used to calculate the total-energy curve of the system as a function of its total magnetic moment and the corresponding DOS features. The cases of V_{Al} and Co_{Sc} are chosen as representatives. The results are shown in Figs. S10 and S12 in the Supplemental Material [32]. These results indicate that the relative stability of the 0/2 μ_B configurations for the V_{Al} and the 0/4 μ_B configurations for Co_{Sc}, as well as the partial density of states feature, are consistent with the PBE results, validating the findings in both sections.

Based on the analysis, we conclude that the relative stability of different TM electronic configurations can be tuned by the polarization field in the mix-phase AlN_3/ScN_3 superlattice. Furthermore, for comparison, we have calculated

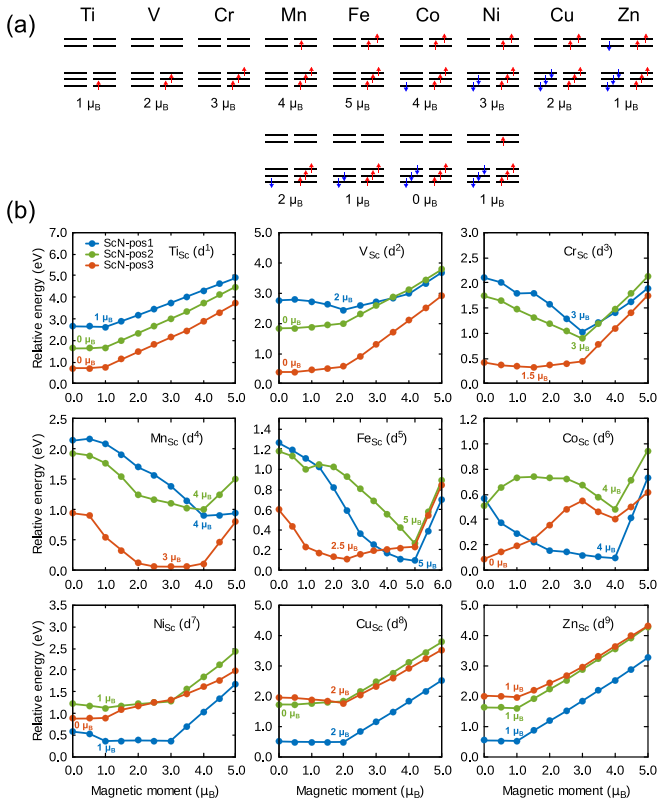

FIG. 4. (a) Electronic configurations for TM dopants under ideal octahedral coordination. (b) Relative energy as a function of the total magnetic moment for TM in different doping positions in the ScN region of mix-phase AlN_3/ScN_3. The stable magnetic moment for each case is labeled.

the electronic configuration of TM dopants in a wurtzite AlN_3/ScN_3 superlattice, which possesses a relatively smaller polarization field. The results are depicted in Figs. S7 and S8 in the Supplemental Material [32]. In this case, the energy curves of different doping positions are similar, indicating that the properties of TM dopants are less affected. These results suggest that a sufficiently strong polarization field is necessary for the effective control of the dopant electronic configuration.

D. Spin interaction between transition-metal pairs in AlN/ScN superlattice

In addition to the individual dopant properties, we demonstrate that the polarization effect can also tune the interaction between different dopants. A typical case is the spin-exchange interaction, which plays a crucial role in determining the performance of a dilute magnetic semiconductor [5,6]. A strong ferromagnetic (FM) coupling between magnetic dopants in a dilute magnetic semiconductor ensures a high Curie temperature and better performance as a spintronic device. However, ferromagnetic coupling between dopants in semiconductors is usually weak.

As illustrated in Fig. 6(a), based on the Goodenough-Kanamori-Anderson rule [51–54], for TM dopants under tetrahedral coordination, the superexchange interactions are antiferromagnetic (AFM) where the virtual electron transfer is between the half-filled *e* states, and they are

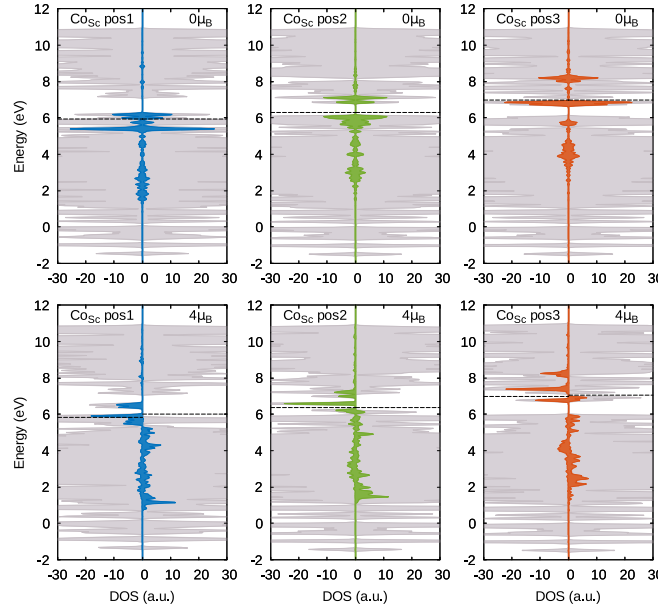

FIG. 5. Total density of states (gray line) and projected density of states of the *d* orbitals of Co_{Sc} in the ScN region of mix-phase AlN_3/ScN_3 at pos1 (blue line), pos2 (green line), and pos3 (red line). The negative and positive values correspond to spin-down and spin-up channels, respectively. The dashed line indicates the Fermi level.

ferromagnetic where the virtual electron transfer is from the half-filled *e* states to the empty t_2 states. Many approaches have been proposed to overcome this drawback; for the case of CrI_3, a two-dimensional ferromagnetic semiconductor, Huang *et al.* [55] have shown that alloying its cation site with tungsten (W) can enhance its ferromagnetic Curie temperature; as the energy level difference between the high-energy empty

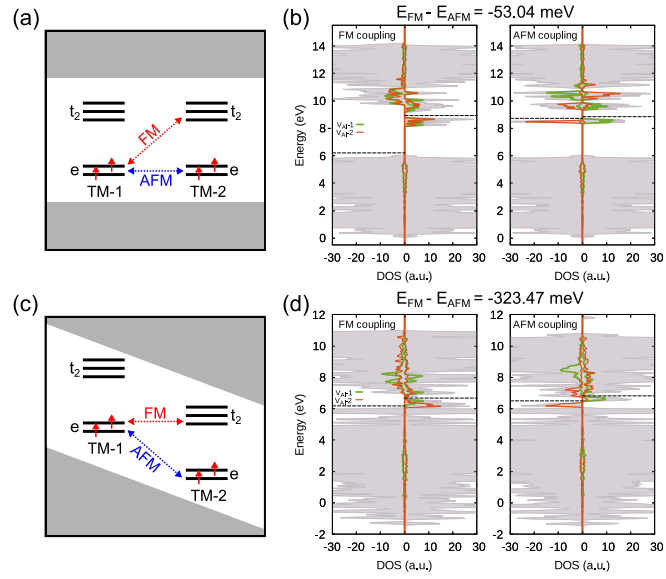

FIG. 6. The schematic spin-exchange mechanism between TM dopants (a) without and (c) with a polarization effect. The total density of states and projected density of states for the *d* orbitals for V_{Al} pairs with ferromagnetic/antiferromagnetic couplings in (b) bulk AlN and (d) the AlN region of mix-phase AlN_3/ScN_3.

states of Cr and the low-energy half-filled states of W is reduced, the ferromagnetic coupling between the adjacent sites is enhanced.

Here we show that the polarization effect can also effectively tune the spin-exchange interaction between dopants; the mechanism is illustrated in Fig. 6(c). Due to the polarization effect, TM dopants experience different electronic potentials, leading to shifts in their energy levels. Consequently, the energy difference between the half-filled e states and the empty t_2 states is reduced, resulting in an enhancement of the FM coupling. As a representative example, we consider the case of vanadium substitution (V_{Al}) in both bulk AlN and the AlN region of mix-phase AlN_3/ScN_3, as V_{Al} exhibits an ideal configuration with half-filled e states and empty t_2 states. We investigate the interaction between a pair of V_{Al} dopants. In bulk AlN, the V_{Al} pair is selected at adjacent cation positions along the [0001] direction, where V_{Al}-2 lies higher than V_{Al}-1 along the [0001] direction. In mix-phase AlN_3/ScN_3, the V_{Al} pair is chosen at adjacent positions, specifically, V_{Al}-pos2 (V_{Al}-1) and V_{Al}-pos3 (V_{Al}-2), using the notation previously employed. The FM and AFM states of the V_{Al} pairs are determined by constraining the alignment of the magnetic moments on the transition metal.

The density of states results and the relative stability of the FM and AFM states for the V_{Al} pair in the bulk AlN and the AlN region of the mix-phase AlN_3/ScN_3 are shown in Figs. 6(b) and 6(d). In the case of the V_{Al} pair in AlN, due to the lack of a polarization effect in bulk AlN, the energy levels of V_{Al}-1 and V_{Al}-2 in AlN lie in a similar region, resulting in a relatively weak FM coupling. The energy of the FM state is 53.04 meV lower than that of the AFM state. In the case of the V_{Al} pair in mix-phase AlN_3/ScN_3, there is an energy level difference between V_{Al}-1 and V_{Al}-2 due to polarization. This leads to enhanced ferromagnetic coupling between the half-filled e and t_2 states, resulting in a stabilized FM coupling configuration. The energy of the FM state is 323.47 meV lower than that of the AFM state. These results demonstrate that the polarization effect can effectively tune the interaction between dopants.

Additionally, we conducted calculations of the spin-exchange couplings for the V_{Al} pair in both bulk AlN and the AlN region of the mix-phase AlN_3/ScN_3 using the LDA and SCAN functionals. The results, as presented in Fig. S11 in the Supplemental Material [32], show consistent trends with those obtained using the PBE functional. Specifically, for both tested functionals, weak ferromagnetic or even antiferromagnetic couplings are observed for V_{Al} pairs in bulk AlN. Meanwhile, in the AlN region of the mix-phase AlN_3/ScN_3 superlattice, ferromagnetic couplings for V_{Al} pairs are enhanced by an order of magnitude. These findings confirm the robustness of the conclusions regarding the influence of the exchange-correlation functional.

E. Formation energy of transition-metal dopant in the AlN/ScN superlattice

For practical applications, it is desirable to know the stability and the compensation effect on a dopant. Here, we consider the cases of V_{Al} and Co_{Sc}, as previously described. We calculate the formation energies of these dopants; the positive and negative charged states are considered. In the charged state calculations, we first compute the total energy as a function of the total magnetic moment to determine the stable electronic configuration. The results are shown in Fig. S6 of the Supplemental Material [32]. Using the total energy of different charged states, we then calculate the formation energy under N-rich conditions, as depicted in Fig. 7. Distinct energy profiles are observed for the same dopant at various doping positions, reflecting the significant built-in polarization in the host material. These energy profiles provide insights into the stability of different charge states of TM dopants.

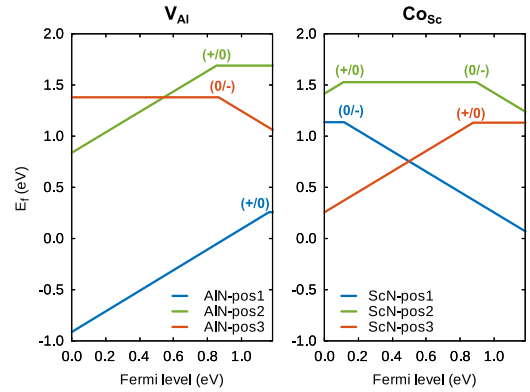

FIG. 7. The formation energies of V_{Al} and Co_{Sc} in mix-phase AlN_3/ScN_3 at the N-rich condition.

For the compensation effect, various factors can contribute, including different types of defects that either donate electrons or holes to the host material. To simplify our analysis, we examine the compensation effect from the perspective of the Fermi level. As illustrated in Fig. 7, for the case of V_{Al} in a charge-neutral state, it is shown that V_{Al}-pos1 and V_{Al}-pos2 exhibit stability in the region near the conduction band maximum, indicating stability primarily in an n-type host. In contrast, for V_{Al}-pos3, the charge-neutral state is stable in the region between the valence band maximum and the middle of the band gap, suggesting stability in a p-type host. Similarly, for the charge-neutral state of Co_{Sc}, it is shown that Co_{Sc}-pos1 exhibits stability in a p-type host, Co_{Sc}-pos2 in an intrinsic-type (i-type) host, and Co_{Sc}-pos3 in an n-type host. These observations provide insights into the compensation mechanisms for V_{Al} and Co_{Sc} dopants within the mix-phase AlN_3/ScN_3 material.

The influence of different exchange-correlation functionals is assessed by comparing the results obtained using the LDA and SCAN functionals. The results are presented in Figs. S12 and S13 of the Supplemental Material [32]. It is shown that the relative stability of the charge-neutral state of V_{Al} and Co_{Sc}, as well as their stable regions within the band gap, exhibit qualitatively similar behavior with the PBE result. This suggests that the overall trends regarding the stability of these dopants remain consistent regardless of the choice of exchange-correlation functional.

IV. CONCLUSION

In summary, our investigation focused on the polarization properties within a mix-phase AlN/ScN superlattice

and its impact on dopant behavior within it. We performed first-principles calculations on the magnetic metastability of individual dopants and the magnetic exchange interactions between different dopants using various types of exchange-correlation functionals. Using the examples of individual Co_{Sc} and V_{Al} pairs in mix-phase AlN_3/ScN_3, we found that the stable magnetic electronic configurations of individual dopants and the magnetic interactions between dopant pairs can both be possibly influenced by the polarization effect. Our results highlight that dopant properties, including their stable magnetic configurations and magnetic interactions, can be significantly tuned by a sufficiently large polarization field. These findings underscore the potential of mix-phase AlN/ScN superlattices with large polarization strength to serve as versatile platforms for achieving polarization modulation of various dopants. Also, the concept presented in this work opens up opportunities for research and technological applications utilizing the polarization effect on doping physics.

ACKNOWLEDGMENTS

This work was supported by the National Key Research and Development Program of China (Grant No. 2023YFB3610400), the National Natural Science Foundation of China (Grants No. 12234018, No. 62121005, and No. 12004378), and the Youth Growth Science and Technology Program of Jilin Province (Grant No. 20220508018RC).

[1] D. J. Norris, A. L. Efros, and S. C. Erwin, Doped nanocrystals, Science **319**, 1776 (2008).
[2] A. Zunger and O. I. Malyi, Understanding doping of quantum materials, Chem. Rev. **121**, 3031 (2021).
[3] T. Shinada, S. Okamoto, T. Kobayashi, and I. Ohdomari, Enhancing semiconductor device performance using ordered dopant arrays, Nature (London) **437**, 1128 (2005).
[4] H. Ohno, Making nonmagnetic semiconductors ferromagnetic, Science **281**, 951 (1998).
[5] K. Sato, L. Bergqvist, J. Kudrnovský, P. H. Dederichs, O. Eriksson, I. Turek, B. Sanyal, G. Bouzerar, H. Katayama-Yoshida, V. A. Dinh, T. Fukushima, H. Kizaki, and R. Zeller, First-principles theory of dilute magnetic semiconductors, Rev. Mod. Phys. **82**, 1633 (2010).
[6] T. Dietl and H. Ohno, Dilute ferromagnetic semiconductors: Physics and spintronic structures, Rev. Mod. Phys. **86**, 187 (2014).
[7] H. Ohno, A. Shen, F. Matsukura, A. Oiwa, A. Endo, S. Katsumoto, and Y. Iye, (Ga,Mn)As: A new diluted magnetic semiconductor based on GaAs, Appl. Phys. Lett. **69**, 363 (1996).
[8] K. Ueda, H. Tabata, and T. Kawai, Magnetic and electric properties of transition-metal-doped ZnO films, Appl. Phys. Lett. **79**, 988 (2001).
[9] M. E. Overberg, C. R. Abernathy, S. J. Pearton, N. A. Theodoropoulou, K. T. McCarthy, and A. F. Hebard, Indication of ferromagnetism in molecular-beam-epitaxy-derived N-type GaMnN, Appl. Phys. Lett. **79**, 1312 (2001).
[10] S. A. Wolf, D. D. Awschalom, R. A. Buhrman, J. M. Daughton, S. von Molnár, M. L. Roukes, A. Y. Chtchelkanova, and D. M. Treger, Spintronics: A Spin-based electronics vision for the future, Science **294**, 1488 (2001).
[11] A. Fert, Nobel lecture: Origin, development, and future of spintronics, Rev. Mod. Phys. **80**, 1517 (2008).
[12] X. Qin, X. Liu, W. Huang, M. Bettinelli, and X. Liu, Lanthanide-activated phosphors based on $4f$-$5d$ optical transitions: Theoretical and experimental aspects, Chem. Rev. **117**, 4488 (2017).
[13] C. Kurtsiefer, S. Mayer, P. Zarda, and H. Weinfurter, Stable solid-state source of single photons, Phys. Rev. Lett. **85**, 290 (2000).
[14] W. F. Koehl, B. B. Buckley, F. J. Heremans, G. Calusine, and D. D. Awschalom, Room temperature coherent control of defect spin qubits in silicon carbide, Nature (London) **479**, 84 (2011).
[15] Z. Zhang and J. T. Yates, Jr., Band bending in semiconductors: Chemical and physical consequences at surfaces and interfaces, Chem. Rev. **112**, 5520 (2012).
[16] K.-M. C. Fu, C. Santori, P. E. Barclay, and R. G. Beausoleil, Conversion of neutral nitrogen-vacancy centers to negatively charged nitrogen-vacancy centers through selective oxidation, Appl. Phys. Lett. **96**, 121907 (2010).
[17] M. V. Hauf, B. Grotz, B. Naydenov, M. Dankerl, S. Pezzagna, J. Meijer, F. Jelezko, J. Wrachtrup, M. Stutzmann, F. Reinhard, and J. A. Garrido, Chemical control of the charge state of nitrogen-vacancy centers in diamond, Phys. Rev. B **83**, 081304(R) (2011).
[18] W. Hu, Z. Li, J. Yang, and J. Hou, Nondecaying long range effect of surface decoration on the charge state of NV center in diamond, J. Chem. Phys. **138**, 034702 (2013).
[19] E. F. Schubert, W. Grieshaber, and I. D. Goepfert, Enhancement of deep acceptor activation in semiconductors by superlattice doping, Appl. Phys. Lett. **69**, 3737 (1996).
[20] P. Kozodoy, M. Hansen, S. P. DenBaars, and U. K. Mishra, Enhanced Mg doping efficiency in $Al_{0.2}Ga_{0.8}N$/GaN superlattices, Appl. Phys. Lett. **74**, 3681 (1999).
[21] K. Jiang, X. Sun, Z. Shi, H. Zang, J. Ben, H. Deng, and D. Li, Quantum engineering of non-equilibrium efficient *p*-doping in ultra-wide band-gap nitrides, Light Sci. Appl. **10**, 69 (2021).
[22] J. Wang, M. Wang, F. Xu, B. Liu, J. Lang, N. Zhang, X. Kang, Z. Qin, X. Yang, X. Wang, W. Ge, and B. Shen, Sub-nanometer ultrathin epitaxy of AlGaN and its application in efficient doping, Light Sci. Appl. **11**, 71 (2022).
[23] J. Simon, V. Protasenko, C. Lian, H. Xing, and D. Jena, Polarization-induced hole doping in wide-band-gap uniaxial semiconductor heterostructures, Science **327**, 60 (2010).
[24] G. Kresse and J. Furthmüller, Efficient iterative schemes for *ab initio* total-energy calculations using a plane-wave basis set, Phys. Rev. B **54**, 11169 (1996).
[25] G. Kresse and J. Furthmüller, Efficiency of *ab initio* total energy calculations for metals and semiconductors using a plane-wave basis set, Comput. Mater. Sci. **6**, 15 (1996).

[26] P. E. Blöchl, Projector augmented-wave method, Phys. Rev. B **50**, 17953 (1994).

[27] G. Kresse and D. Joubert, From ultrasoft pseudopotentials to the projector augmented-wave method, Phys. Rev. B **59**, 1758 (1999).

[28] D. M. Ceperley and B. J. Alder, Ground state of the electron gas by a stochastic method, Phys. Rev. Lett. **45**, 566 (1980).

[29] J. P. Perdew, K. Burke, and M. Ernzerhof, Generalized gradient approximation made simple, Phys. Rev. Lett. **77**, 3865 (1996).

[30] J. Sun, A. Ruzsinszky, and J. P. Perdew, Strongly constrained and appropriately normed semilocal density functional, Phys. Rev. Lett. **115**, 036402 (2015).

[31] Y. Fu and D. J. Singh, Density functional methods for the magnetism of transition metals: SCAN in relation to other functionals, Phys. Rev. B **100**, 045126 (2019).

[32] See Supplemental Material at http://link.aps.org/supplemental/10.1103/PhysRevB.110.035206 for additional computation results with PBE functional (Sec. I) and benchmark of different exchange-correlation functionals (Sec. II).

[33] C. Freysoldt, B. Grabowski, T. Hickel, J. Neugebauer, G. Kresse, A. Janotti, and C. G. Van de Walle, First-principles calculations for point defects in solids, Rev. Mod. Phys. **86**, 253 (2014).

[34] C. Freysoldt, J. Neugebauer, and C. G. Van de Walle, Fully *ab initio* finite-size corrections for charged-defect supercell calculations, Phys. Rev. Lett. **102**, 016402 (2009).

[35] C. Freysoldt, J. Neugebauer, and C. G. Van de Walle, Electrostatic interactions between charged defects in supercells, Phys. Status Solidi B **248**, 1067 (2011).

[36] M. Noor-A-Alam, O. Z. Olszewski, and M. Nolan, Ferroelectricity and large piezoelectric response of AlN/ScN superlattice, ACS Appl. Mater. Interfaces **11**, 20482 (2019).

[37] Z. Jiang, C. Paillard, D. Vanderbilt, H. Xiang, and L. Bellaiche, Designing multifunctionality via assembling dissimilar materials: Epitaxial AlN/ScN superlattices, Phys. Rev. Lett. **123**, 096801 (2019).

[38] H. Zang, Z. Shi, M. Liu, Y. Jia, K. Jiang, J. Ben, Y. Chen, S. Lv, X. Sun, and D. Li, Tunable piezoelectric and ferroelectric responses of $Al_{1-x}Sc_xN$: The role of atomic arrangement, Sci. China Phys. Mech. Astron. **66**, 277711 (2023).

[39] Z. Y. Al Balushi, K. Wang, R. K. Ghosh, R. A. Vilá, S. M. Eichfeld, J. D. Caldwell, X. Qin, Y.-C. Lin, P. A. DeSario, G. Stone, S. Subramanian, D. F. Paul, R. M. Wallace, S. Datta, J. M. Redwing, and J. A. Robinson, Two-dimensional gallium nitride realized via graphene encapsulation, Nat. Mater. **15**, 1166 (2016).

[40] W. Wang, Y. Zheng, X. Li, Y. Li, H. Zhao, L. Huang, Z. Yang, X. Zhang, and G. Li, 2D AlN layers sandwiched between graphene and Si substrates, Adv. Mater. **31**, 1803448 (2019).

[41] R. Yan, G. Khalsa, S. Vishwanath, Y. Han, J. Wright, S. Rouvimov, D. S. Katzer, N. Nepal, B. P. Downey, D. A. Muller, H. G. Xing, D. J. Meyer, and D. Jena, GaN/NbN epitaxial semiconductor/superconductor heterostructures, Nature (London) **555**, 183 (2018).

[42] F. Bernardini and V. Fiorentini, Macroscopic polarization and band offsets at nitride heterojunctions, Phys. Rev. B **57**, R9427 (1998).

[43] X. Y. Cui, D. J. Carter, M. Fuchs, B. Delley, S. H. Wei, A. J. Freeman, and C. Stampfl, Continuously tunable band gap in GaN/AlN (0001) superlattices via built-in electric field, Phys. Rev. B **81**, 155301 (2010).

[44] S. Massidda, B. I. Min, and A. J. Freeman, Interface phenomena at semiconductor heterojunctions: Local-density valence-band offset in GaAs/AlAs, Phys. Rev. B **35**, 9871 (1987).

[45] S. Picozzi, A. Continenza, and A. J. Freeman, Electric fields and valence-band offsets at strained [111] heterojunctions, Phys. Rev. B **55**, 13080 (1997).

[46] X. Y. Cui, B. Delley, A. J. Freeman, and C. Stampfl, Magnetic metastability in tetrahedrally bonded magnetic III-Nitride semiconductors, Phys. Rev. Lett. **97**, 016402 (2006).

[47] L. Weston, X. Y. Cui, S. P. Ringer, and C. Stampfl, Bistable magnetism and potential for voltage-induced spin crossover in dilute magnetic ferroelectrics, Phys. Rev. Lett. **114**, 247601 (2015).

[48] H. Raebiger, S. Lany, and A. Zunger, Charge self-regulation upon changing the oxidation state of transition metals in insulators, Nature (London) **453**, 763 (2008).

[49] J. S. Griffith and L. E. Orgel, Ligand-field theory, Qtrly. Rev. Chem. Soc. **11**, 381 (1957).

[50] M.-H. Whangbo and H. Xiang, Magnetic properties from the perspectives of electronic Hamiltonian, in *Handbook of Solid State Chemistry* (Wiley, New York, 2017), Chap. 10, pp. 285–343.

[51] P. W. Anderson, Antiferromagnetism. Theory of superexchange interaction, Phys. Rev. **79**, 350 (1950).

[52] J. B. Goodenough, Theory of the role of covalence in the perovskite-type manganites [La, M(II)]MnO_3, Phys. Rev. **100**, 564 (1955).

[53] J. Kanamori, Superexchange interaction and symmetry properties of electron orbitals, J. Phys. Chem. Solids **10**, 87 (1959).

[54] J. B. Goodenough, Goodenough-Kanamori rule, Scholarpedia **3**, 7382 (2008).

[55] C. Huang, J. Feng, F. Wu, D. Ahmed, B. Huang, H. Xiang, K. Deng, and E. Kan, Toward intrinsic room-temperature ferromagnetism in two-dimensional semiconductors, J. Am. Chem. Soc. **140**, 11519 (2018).